Chemical Engineering Journal 435 (2022) 135033

Contents lists available at ScienceDirect

Chemical Engineering Journal

journal homepage: www.elsevier.com/locate/cej

Enhanced adsorption and visible-light photocatalytic degradation of toluene by CQDs/UiO-66 MOG with hierarchical pores

Jiajun Yu [a,b], Xiao Wang [a,*], Lu Chen [a], Guanhong Lu [a], Gansheng Shi [a], Xiaofeng Xie [a], Yan Wang [a], Jing Sun [a,*]

[a] State Key Lab of High Performance Ceramics and Superfine Microstructure, Shanghai Institute of Ceramics, Chinese Academy of Sciences, 585 Heshuo Road, Shanghai 201899, China

[b] University of Chinese Academy of Sciences, 19 (A) Yuquan Road, Beijing 100049, China

ARTICLE INFO

Keywords:
CQDs/UiO-66 MOG
Toluene
Photocatalytic oxidation

ABSTRACT

The development of photocatalytic materials with both promising adsorption capacity and high visible-light activity is essential for the highly-efficient and stable photocatalytic degradation of toluene. In this work, a series of carbon quantum dots (CQDs) decorated UiO-66 metal–organic-frameworks gel (MOG) composites (CQDs/UiO-66 MOG) with hierarchical pore structures were prepared. The introduction of CQDs effectively improved the light utilization and promoted the separation of photo-induced electrons and holes, which were beneficial for the generation of active free radicals. Besides, benefiting from the hierarchical pore structure of UiO-66 MOG and the new adsorption sites provided by CQDs, 0.5 wt% CQDs/UiO-66 MOG showed a high toluene adsorption capacity (29.06 μmol/g) and its enhanced degradation efficiency for toluene was 4.4 times higher than that of pristine UiO-66 MOG. Both in-situ Fourier transform infrared (FTIR) and Gas Chromatography–Mass Spectrometer (GC–MS) were conducted to give the possible degradation pathways. Toluene was firstly converted into xylene and benzene, and then degraded into acids, aldehydes, alcohols before fully mineralized into carbon dioxide. A relatively high CO_2 conversion ratio (85%) of toluene was obtained when applying 0.5 wt% CQDs/UiO-66 MOG as the photocatalyst, together with less intermediates detected, confirming the positive role of CQDs decoration in the effective mineralization of toluene. This work sheds new light on MOG material optimization and degradation of low-concentration flowing toluene.

1. Introduction

With the development of industrialized society, environmental problems have become increasingly severe. The monitoring and treatment of pollutants in the environment have already attracted extensive attention. Among them, volatile organic compounds (VOCs) have been detected in both indoor and outdoor air [1]. VOCs have pungent smell, irritation to the skin and mucous membrane and carcinogenicity, which harm human health. In addition, VOCs are also essential precursors to form particulate pollutants (such as PM2.5 and O_3) during photochemical reactions. Photocatalysts can decompose pollutants by using photon energy under the irradiation of light, which has excellent application prospects in the removal of typical VOCs [2]. Due to the large-scale application in the coating industry, aromatic hydrocarbons are among the major VOCs in urban air, among which toluene is the representative aromatic hydrocarbon. The elimination of toluene is meaningful for city air purification. However, the photocatalytic elimination of toluene still faces many difficulties. On the one hand, the affinity of common applied TiO_2 for toluene is usually poor due to their nonpolar structure, which impedes the capture of gaseous toluene. On the other side, toluene is difficult to be degraded due to the stable benzene rings, which may cause the deactivation of photocatalysts [3]. Therefore, there is an urgent need to develop photocatalysts with both high adsorption and photocatalytic ability for the purification of toluene.

Metal organic frameworks (MOFs), as a newly emerging crystalline coordination polymer with high-porosity, have attracted extensive attention from researchers due to their large specific surface area, adjustable porosity, and designable structure [4,5]. At present, it has been widely used in medicine and drug delivery [6], adsorption [7], gas storage/separation [8], sensing [9], catalysis [10], proton conductor [11] and electrochemistry [12]. In 2007, Francesc and colleagues [13]

* Corresponding authors.
E-mail addresses: wangxiao@mail.sic.ac.cn (X. Wang), jingsun@mail.sic.ac.cn (J. Sun).

https://doi.org/10.1016/j.cej.2022.135033
Received 16 November 2021; Received in revised form 29 January 2022; Accepted 30 January 2022
Available online 4 February 2022

used MOF-5 as a photocatalyst to degrade phenol, and discovered that MOFs as semiconductor materials had great potential in photovoltaic applications. As a result, more and more researchers have explored the application of MOFs in the field of photocatalysis. Zhang et al. [14] used porphyrin zirconium MOFs and MOF-525 (Zn) as photocatalysts for PET-RAFT polymerization, and pointed out that changing the size and surface area of MOFs could significantly affect the polymerization rate of PET-RAFT. Hu et al. [15] incorporated MOF for hydrogen evolution reaction into the hydrophobic layer of liposomes, and for water oxidation reaction into the hydrophilic layer of liposomes, so as to effectively separate charges and the catalysts facilitated overall photocatalytic water splitting. MOFs are also widely used in the adsorption and photocatalytic degradation of gas pollutants due to their large specific surface area and photocatalytic ability. Chen et al. [16] synthesized MIL-100(Fe)/α-Fe_2O_3 by hydrothermal method, and used it in the highly efficient degradation of o-xylene under visible light. Cheng et al. [17] synthesized NH_2-MIL-125 (Ti) with different proportions of {0 0 1} and {1 1 1} planes and used it in photocatalytic CO_2 reduction. However, for gas-phase photocatalysis, the microporous structure of MOFs may not be conducive to the adsorption of macromolecules and the mass transfer of these guest molecules to reach active sites, which limits its application in the industry [18].

Metal-organic-frameworks gel (MOGs) are hierarchical porous materials with the same chemical composition as the corresponding MOFs. Unlike typical MOFs, MOGs are colloidal networks composed of discrete crystalline nanoparticles [18]. In addition, MOGs have both micro- and mesopores, compared with the micropores of MOFs. This hierarchical pore structure is conducive to the VOCs' adsorption and mass transfer, and has great potential in gas phase photocatalysis [19]. UiO-66 (Zr) MOF, not only has the advantages of the large specific surface area and adjustable chemical structure that most MOFs have, but also has rare advantages such as excellent air stability and thermal stability [20], which is conducive to the persistent degradation of gaseous pollutants. Bi et al. [21] prepared Pd/UiO-66 by an ethylene glycol reduction method for the thermal catalytic degradation of toluene. Zhang et al. [22] prepared TiO_2/UiO-66 by a solvothermal method, which can degrade toluene under UV light. However, none of these UiO-66 based materials show promising performance under visible light due to the wide band gap of UiO-66. Besides, unlike the fully crystalline MOF counterparts, UiO-66 MOG usually shows relatively poor conductivity due to the existence of defects and the colloidal structure, which shortens the life-time of photo-generated electron-hole pairs and impedes the generation of oxidative radicals.

Carbon quantum dots (CQDs) are zero-dimensional (0D) like carbon-based materials with low resistance, good chemical stability and strong light trapping ability. Its synthesis methods include: a) breaking macromolecular carbon materials into micromolecular carbon nanoparticles through physical or chemical methods; b) organic molecules are used as precursors (carbon sources) [23]. As an electron acceptor, CQDs can effectively inhibit the recombination of electron-hole pairs when combined with other photocatalysts [24]. CQDs can also act as photosensitizer under long wavelength light irradiation due to their up-conversion characteristics and photoluminescence characteristics, which improve light utilization efficiency and enhance photocatalytic activity of catalysts [25,26].

Based on the above discussion, a series of CQDs/UiO-66 MOG composite materials were synthesized to achieve the visible-light-driven photocatalytic degradation of toluene. Benefiting from the mesopores of UiO-66 MOG and the new active sites provided by CQDs, in-situ Fourier transform infrared (FTIR) and adsorption results indicated that CQDs/UiO-66 MOG displayed a high adsorption capacity for toluene. The up-conversion effect of CQDs and Schottky junction formed between the two components enhanced the light utilization and promoted the separation of electron-hole pairs. CQDs/UiO-66 MOG could generate more free radicals for the oxidative degradation. Furthermore, the possible degradation pathway and mechanism of toluene were proposed by in-situ FTIR and Gas Chromatography-Mass Spectrometer (GC–MS) analyses. The CO_2 conversion was also analyzed, further confirming the potential of CQDs/UiO-66 MOG in the photocatalytic elimination of toluene. This study provided new ideas for the modification of MOG materials and the treatment of gaseous organic pollutants.

2. Experimental section

2.1. Chemicals and materials

Citric acid monohydrate ($C_6H_8O_7{\cdot}H_2O$, 99.5%) and urea (CH_4N_2O, ≥99.0%) were purchased from China Sinopharm Chemical Reagent Co., Ltd. Zirconium tetrachloride ($ZrCl_4$, 98.0% +), tert-butyl alcohol (TBA, $C_4H_{10}O$, 99.5%), 1,4-benzoquinone (PBQ, $C_6H_4O_2$, 99.0%), terephthalic acid (BDC, $C_8H_6O_4$, 99.0%) and N,N-dimethylformamide (DMF, C_3H_7NO, 99.5%) were purchased from Adamas Corporation. Sodium oxalate ($Na_2C_2O_4$, 99.8%) and 2,2,6,6-tetramethyl-1-piperidinyloxy (TEMPO, $C_9H_{18}NO$, 98.0%) were purchased from Shanghai Aladdin Biochemical Technology Co., Ltd. 5,5-Dimethyl- 1-Pyrroline N-Oxide (DMPO, $C_6H_{11}NO$, 99.0%) was purchased from Dojindo Laboratory. Ethyl alcohol (C_2H_5OH) was provided by Shanghai Lingfeng Chemical Reagent Co., Ltd. Deionized (DI, H_2O) water was provided by the Milli-Q system manufactured by Shanghai Tongdi Scientific Instruments Co., Ltd. The chemicals used in the experiment were analytically pure and could be used without further purification.

2.2. Samples preparation

2.2.1. Synthesis of CQDs

According to the previous report, CQDs were synthesized by a hydrothermal method [27]. 1.0 g of citric acid and 1.0 g of urea were dissolved in 15 mL of DI. The solution was kept at 180 °C for 6 h for hydrothermal reaction. After being cooled to room temperature, the obtained product was centrifuged at a speed of 12,000 r/min for 20 min, and the upper layer solution was placed in a drying box and dried at 80 °C for 10 h to obtain a black solid CQDs.

2.2.2. Synthesis of UiO-66 MOG

UiO-66 MOG was prepared by an improved hydrothermal synthesis method [28]. 0.4664 g of $ZrCl_4$ was dissolved in 25 mL of DMF and 2 mL of DI, and then the mixed solution was sonicated until dissolved. Then 0.3223 g of BDC was dissolved in the above solution, followed by sonication for 15 min and stirred for 2 h. Afterwards, the solution was put into a 50 mL Teflon-lined autoclave for hydrothermal reaction, and kept at 120 °C for 24 h. After being cooled to room temperature, the product was washed with DMF and ethanol for 3 times separately, and then dried in a vacuum environment at 100 °C for 12 h.

2.2.3. Synthesis of CQDs/UiO-66 MOG

The UiO-66 MOG obtained after the hydrothermal reaction was washed 3 times with DMF and then dispersed in ethanol, designated as solution A. The CQDs were dispersed in water and denoted as solution B (5 mg/mL). 0.2, 0.5, 1.0 mL of solution B was added dropwise into solution A under stirring. The mixture was then stirred for another 2 h. The product was then centrifuged and washed 3 times with ethanol and dried under vacuum at 100 °C for 12 h. Finally, samples x wt% CQDs/UiO-66 MOG (x = 0.2, 0.5, 1.0) were obtained.

2.3. Characterization

The surface morphology of the samples was observed by a field emission scanning electron microscope (SEM, Magellan 400) which was built by FEI Company. The size of CQDs was observed by a transmission electron microscope (TEM, SU9000, Hitachi). The structures of the samples were characterized by a high-resolution powder X-ray diffractometer (XRD, D8 ADVANCE) produced by Bruker, Germany. The

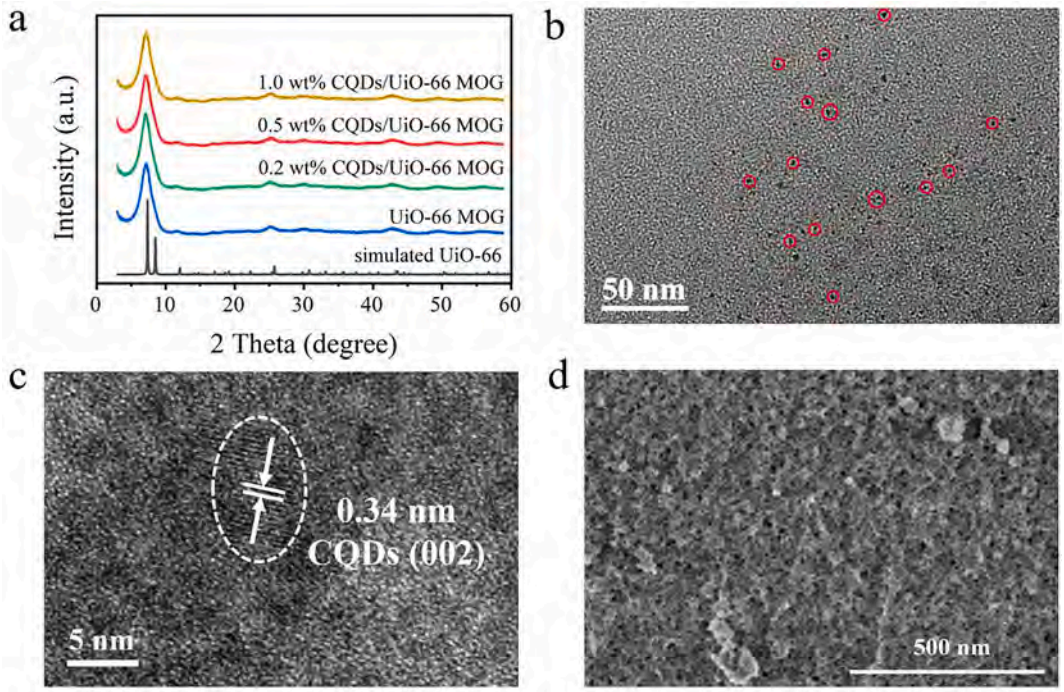

Fig. 1. (a) XRD patterns of CQDs/UiO-66MOG catalysts with different CQDs content. (b) The TEM image of CQDs. The (c) HRTEM image and (d) SEM image of 0.5 wt% CQDs/UiO-66 MOG.

scanning angle of X-ray which used Cu Kα irradiation (λ = 0.15418 nm) ranged from 3° to 60°, and the scanning speed was 2° per minute. The specific surface area and pore structure of the samples were measured by the fully automatic four-station specific surface pore size analyzer (BET, Quadrasorb SI) which was manufactured by Quanta Instruments. The surface valence state analysis of the samples was conducted with an X-ray photoelectron spectrometer (XPS, ESCAlab250) which was manufactured by Thermo Fisher Scientific. The ultraviolet–visible (UV–vis) absorption spectra, which characterized the light absorption characteristics of the samples, were measured by a ultraviolet–visible-near infrared spectrophotometer (Perkin Elmer, model LAMBDA 1050). The photoluminescence spectra (PL), which indicated the degree of photogenerated carrier recombination, were measured by the luminescence spectrometer (model LS 55, Perkin Elmer). The transient photocurrent tests, which indicated the samples' ability to generate photogenerated carriers, were measured by an electrochemical workstation (Shanghai CH Instruments Inc, model Chi 650B). 1 mol/L NaCl solution was prepared as the electrolyte. The established three-electrode system used Ag/AgCl as the reference electrode, the sample as the working electrode and the platinum sheet as the counter electrode. The sample was dissolved in ethanol and spin-coated on FTO conductive glass (25 mm × 15 mm) by a homogenizer. Fourier transform infrared (FTIR) spectra were obtained by using a Thermo Fisher iN10 iZ10 infrared spectrophotometer with KBr as the reference and a deuterated triglycine sulfate detector (DTGS). In-situ FTIR was carried out on the Shimadzu IRTracer-100 instrument, equipped with a mercury cadmium telluride (MCT) detector cooled by liquid nitrogen. A diffuse reflection accessory and a high temperature reaction chamber (both from Harrick Scientific Products Inc.) are coupled with the in-situ FTIR equipment to study the adsorption process of toluene. The FTIR signal of the photocatalyst itself has been subtracted as the background.

2.4. Photocatalytic performance measurements

This work was tested in an automatic continuous gas intake reactor, as shown by Scheme S1 in the supporting information. 0.5 mg photocatalyst was coated on a glass slide (15.0 cm × 7.5 cm) and then placed in a reaction chamber covered with quartz plate. A 250 W xenon lamp was selected as the light source, which was placed directly 30 cm above the reaction chamber. A piece of UV cut off filter (λ > 420 nm) was placed between the light source and the reaction chamber. Toluene (10 ppm) was selected as toxic gas to conduct photocatalytic degradation experiments. The air generated by a three-in-one generator passed through a humidification tank to bring water into the reaction chamber and then mixed with VOC in a gas mixing tank. The mixed gas entered the reaction chamber and reacted with the catalyst. The variation in the concentration of target pollutants was characterized with a gas chromatograph. The humidification tank can regulate the humidity, making the test parameters closer to the real application environment.

Then, the photocatalytic degradation experiment was started. First, in a dark environment, toluene with a flow rate of 20 sccm passed over the surface of the catalyst until the catalyst reached an adsorption–desorption equilibrium. Then the light was turned on for illumination, and toluene concentration was detected by gas chromatograph every 10 min. The adsorption capacity (A_c) of VOC was calculated by equation:

$$A_C = C_0 \times v \times \left\{ \left[\int_0^t \left(1 - \frac{C}{C_0}\right) dt \right]_{catalyst} - \left[\int_0^t \left(1 - \frac{C}{C_0}\right) dt \right]_{blank} \right\} \times (M \times m)^{-1}$$

The degradation efficiency η of the catalyst was calculated according to the following formula:

$$\eta = \frac{C_0 - C}{C_0} \times 100\%$$

$$\text{theoretical } CO_2 \text{ production amount} = C_0 \times \eta \times N$$

$$CO_2 \text{ conversion ratio} = \frac{C_{tCO_2}}{C_0 \times \eta \times N} \times 100\%$$

where C_0 represents the initial concentration of VOC, v represents the flow rate of VOC, C represents the actual concentration of VOC, M represents the molar mass of VOC, m represents the mass of the catalyst, N represents the number of C atoms in a single VOC molecule and $Ctco_2$

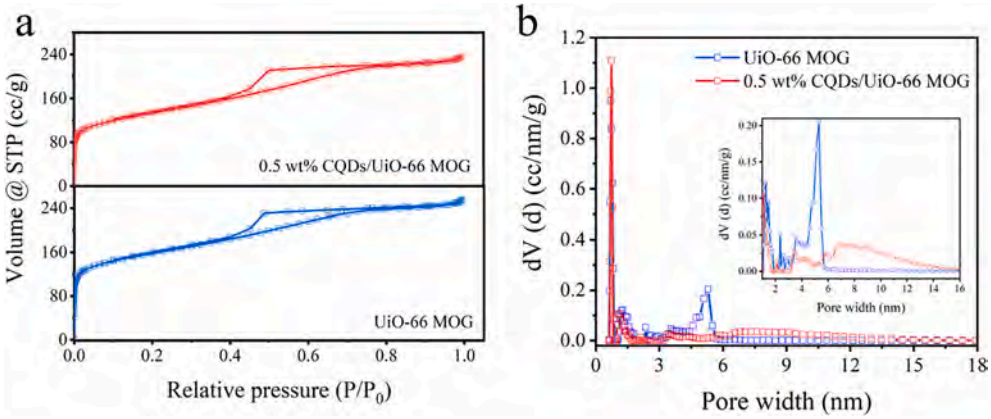

Fig. 2. (a) N_2 adsorption–desorption isotherms at 77 K and (b) pore size distributions of UiO-66 MOG and 0.5 wt% CQDs/UiO-66 MOG.

represents the concentration of CO_2 detected at t min of the PCO reaction.

2.5. ESR tests (Oxygen vacancies and free radicals)

20 mg samples were weighed and oxygen vacancies were measured through an electron spin resonance (ESR) test (JES-FA200 spectrometer). The detection of •OH, $•O_2^-$were also carried out on the JES-FA200 spectrometer. Specifically, 4 mg sample was dissolved in 2 mL DI or ethanol. 100 μL of the solution was taken out and 10 μL DMPO was added into it. DI and ethanol were applied as the solvent to measure the content of •OH, $•O_2^-$, respectively. ESR tests were performed before and after visible-light illumination ($\lambda > 420$ nm) for 5 min.

3. Results and discussion

3.1. Characterization of morphology and structure

Fig. 1a shows the XRD patterns of the different catalysts. The peak positions of UiO-66 MOG were consistent with the simulated XRD

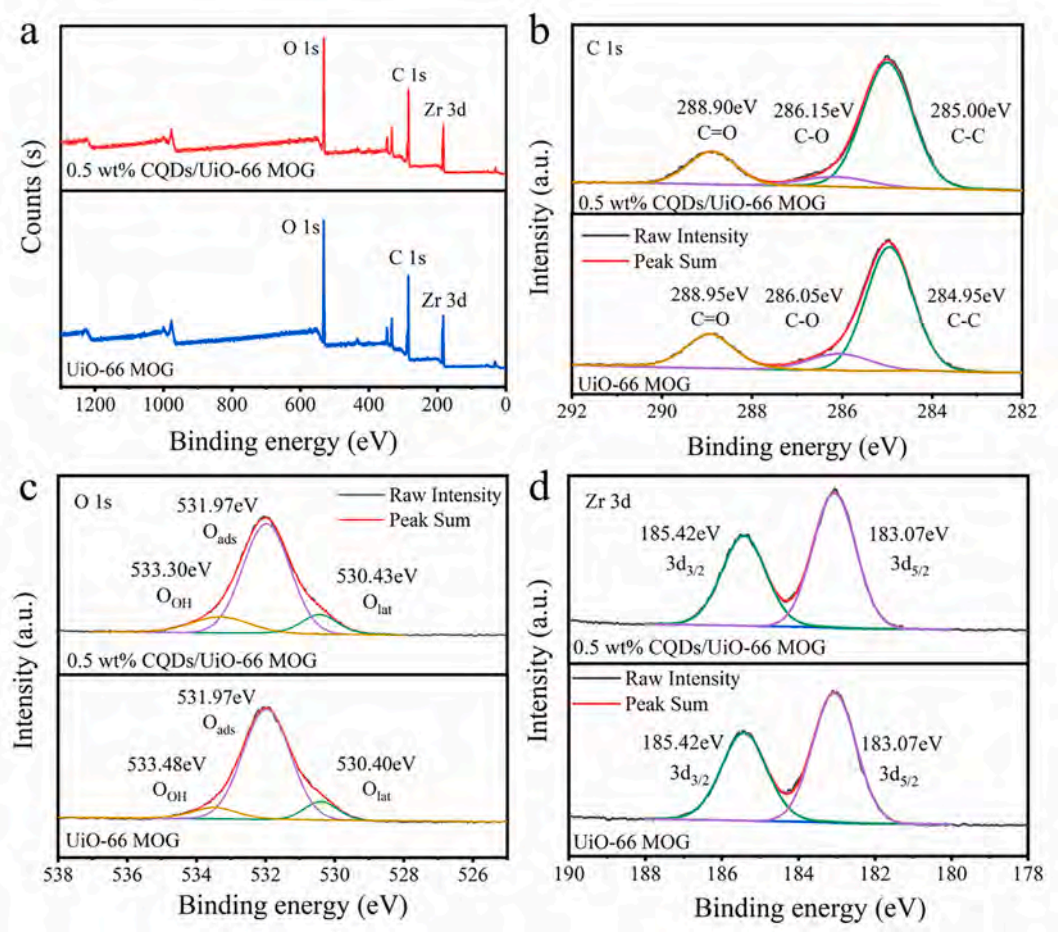

Fig. 3. (a) XPS survey spectrum and (b–d) Corresponding high resolution XPS spectra of C 1 s (b), O 1 s (c), Zr 3d (d) of UiO-66 MOG and 0.5 wt% CQDs/UiO-66 MOG.

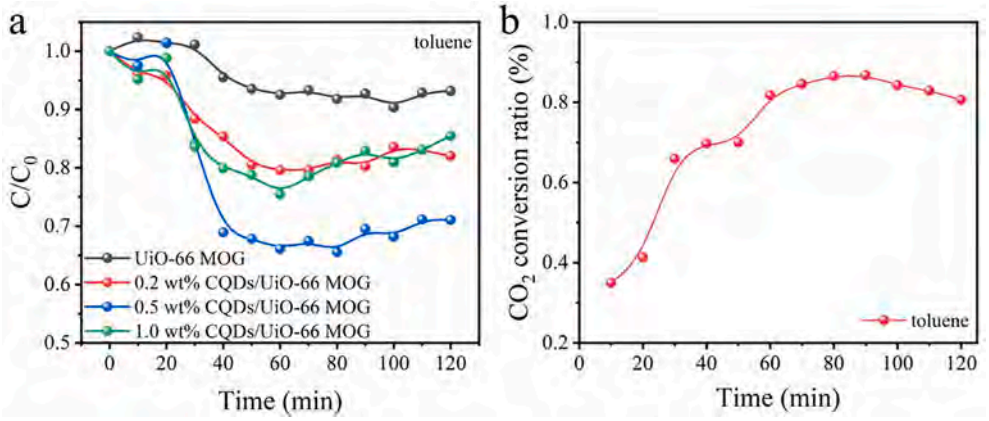

Fig. 4. (a) The toluene degradation curves of 0.05 g photocatalysts under visible light. (b) The CO_2 conversion ratio of toluene degraded by 0.5 wt% CQDs/UiO-66 MOG.

pattern of UiO-66 [29]. However, due to the relatively small size of crystals in UiO-66 MOG, its XRD profile shows broad peaks instead of sharp ones observed in the simulated pattern [30]. After adding CQDs, the peak positions of UiO-66 MOG did not change significantly, confirming that CQDs did not influence the intrinsic structure or the crystallinity of UiO-66 MOG. No peak for CQDs was observed in the XRD pattern of the composites, which could be attributed to the low doping amount of CQDs.

According to high-resolution transmission electron microscopy (HRTEM) results, the spherical CQDs with an average size of about 4–5 nm were successfully synthesized in this work (Fig. 1b, Fig. S1). As given by the HRTEM image of the composite (Fig. 1c), the interplanar spacing of 0.34 nm, which represents the (0 0 2) crystal plane of CQDs [31], could be observed in 0.5 wt% CQDs/UiO-66 MOG, confirming the successful implantation of CQDs. In order to further confirm that CQDs were loaded on UiO-66 MOG, the FTIR spectra (Fig. S2) were carried out. Some characteristic peaks of CQDs, including the C═C bonds in the skeleton ring, overlapped with the ones of UiO-66 MOG and cannot be distinguished such as 1400 cm^{-1} (C—O) and 1580 cm^{-1} (C═C) [32] in Fig. S2. In addition, the characteristic peaks of CQDs in CQDs/UiO-66 MOG are not obvious because the doping amount of CQDs was small. However, the new peak was found at 1248 cm^{-1} (C—H) for CQDs/UiO-66 MOG, which was ascribed to the appearance of CQDs [33], confirming that CQDs were effectively loaded on UiO-66 MOG. Fig. S3 shows the surface morphology of UiO-66 MOG. Unlike the UiO-66 MOF nanoparticles reported previously [21,34], the as-synthesized UiO-66 MOG shows a monolith structure with a rich pore structure on the surface, which may provide channels for the adsorption and migration of target molecules [35]. The SEM image of 0.5 wt% CQDs/UiO-66 MOG (Fig. 1d) shows that the doping of CQDs did not significantly change the morphology of UiO-66 MOG.

Fig. 2a shows the N_2 adsorption–desorption isotherm curves. Both UiO-66 MOG and 0.5 wt% CQDs/UiO-66 MOG show type IV curves, indicating the existence of mesopores. The distribution of pore size in the samples was also analyzed. As shown by Fig. 2b, the irregular accumulation of nanoparticles in UiO-66 MOG resulted in a hierarchical porous structure with both micropores (< 2 nm) and mesopores (ranging from 2 ~ 16 nm). The hierarchical pore structure can greatly reduce the mass transfer limitation and facilitate the adsorption of o-xylene (theoretical size = 0.306 nm) [16 28]. The sample modified with CQDs still maintained the hierarchical porous structure of MOG. However, the volume of mesopores (3–6 nm) was slightly decreased due to the partially occupation of mesopores by CQDs. Similar results could be observed in the Brunauer, Emmett and Teller specific surface area (BET-SSA) (Table S1). The specific surface area decreased from 567.2 m^2/g (UiO-66 MOG) to 465.8 m^2/g of 0.5 wt% CQDs/UiO-66 MOG.

XPS provided information on the element composition, chemical valence and chemical environment of CQDs/UiO-66 MOG (Fig. 3). Fig. 3b shows the C 1s spectrum of UiO-66 MOG. The spectrum of C 1s matched three peaks, which are C—C (284.95 eV), C—O (286.05 eV) and C═O (288.95 eV) [36]. After adding CQDs, the binding energy of C—O and C—C slightly increased, while the peak of C═O shifted to the low energy side. This phenomenon might be attributed to the interaction between CQDs and the organic linkers in UiO-66 MOG. Fig. 3c shows that the O 1s of UiO-66 MOG contains three peaks at 530.33 eV, 531.93 eV and 533.26 eV, which are attributed to lattice oxygen (O_{lat}), adsorbed oxygen (O_{ads}) and surface hydroxyl (O_{OH}) [21]. Unlike the circumstance of O_{lat} and O_{ads}, whose characteristic peaks did not move after the addition of CQDs, a blue shift could be observed in the peak of O_{OH}, meaning that the introduction of CQDs may influence the adsorption of water. Fig. 3d shows the Zr 3d spectrum of UiO-66 MOG, which can be deconvoluted into two peaks with binding energies at 183.07 eV ($3d_{5/2}$) and 185.42 eV ($3d_{3/2}$) [37]. Adding CQDs did not significantly change the chemical environment of zirconium.

3.2. Photocatalytic degradation performance of gaseous VOCs

Fig. 4a shows the degradation curves of toluene for different samples under visible light irradiation. The degradation efficiencies are arranged from high to low as follows: 0.5 wt% CQDs/UiO-66 MOG (35%) > 1.0 wt % CQDs/UiO-66 MOG (22%) > 0.2 wt% CQDs/UiO-66 MOG (20%) > UiO-66 MOG (8%). Among all the samples, 0.5 wt% CQDs/UiO-66 MOG shows the best performance, the degradation efficiency was almost 4.4 times of the pure UiO-66 MOG. However, when further increasing the amount of CQDs, the performance decreased. The excessive CQDs possibly work as carrier recombination centers or influence the adsorption of VOCs by occupying active sites and blocking the micropores. In order to explore the versatility of the samples towards the photocatalytic degradation of aromatic compounds, the degradation of single o-xylene and single styrene under visible light were also conducted (Fig. S4). Among all the samples, 0.5 wt% CQDs/UiO-66 MOG shows the highest degradation efficiency towards both o-xylene (44%) and styrene (29%), further confirming the promotion effect of CQDs decoration on the photocatalytic performance of UiO-66 MOG. In order to clarify the conversion degree of VOCs involved in degradation into CO_2, the real-time CO_2 conversion ratio during the degradation process is shown in Fig. 4b and Fig. S4c. The 0.5 wt% CQDs/UiO-66 MOG showed CO_2 conversion ratio for single toluene (85%), o-xylene (86%) and styrene (30%). Moreover, the comparison with other references regarding the degradation and CO_2 conversion of toluene was conducted (Table S2). Compared with other photocatalysts reported previously, this work achieved the effective degradation and high CO_2 conversion of low-concentration flowing toluene under visible light.

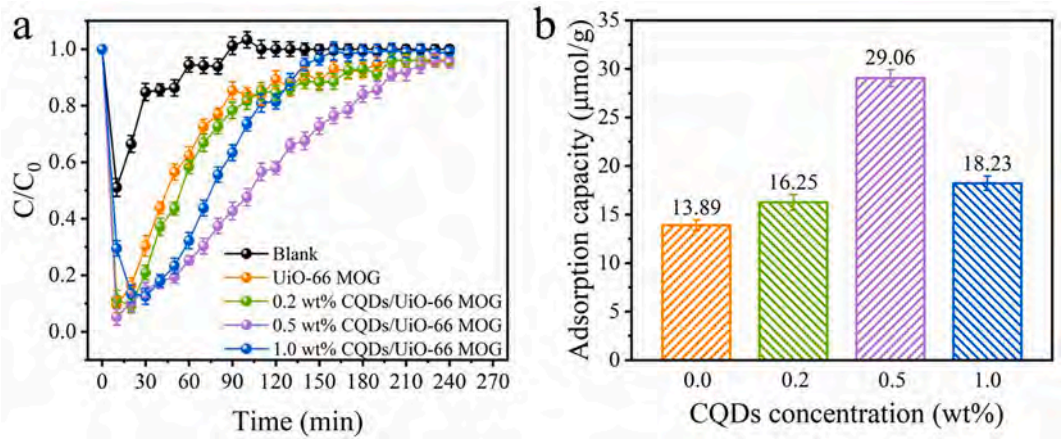

Fig. 5. (a) Dynamic adsorption curves and (b) Adsorption capacities (μmol/g) histograms of UiO- 66 MOG and CQDs/UiO-66 MOG composites towards gaseous toluene under the dark condition.

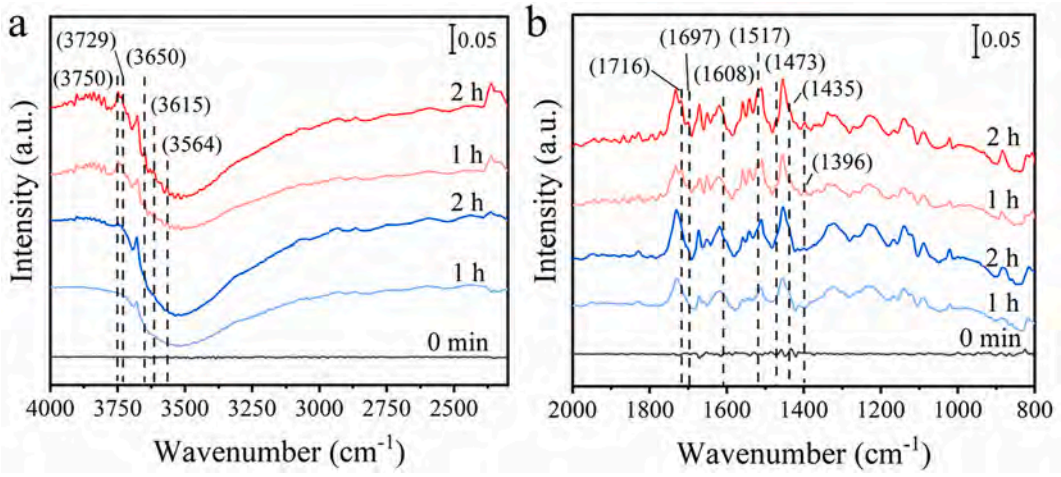

Fig. 6. In-situ FTIR differential spectra of toluene adsorption by catalysts in the range of (a) 4000 – 2300 cm^{-1} and (b) 2000 – 800 cm^{-1}. (Red curves: 0.5 wt% CQDs/UiO-66 MOG, blue curves: UiO-66 MOG. The signal of UiO-66 MOG and 0.5 wt% CQDs/UiO-66 MOG were subtracted, respectively.) (For interpretation of the references to colour in this figure legend, the reader is referred to the web version of this article.)

3.3. Adsorption capacity of catalysts to gaseous toluene

As the adsorption of VOCs by the catalyst is the first step of the photocatalytic oxidation (PCO) of gaseous pollutants [38], the adsorption capacities of the as-synthesized photocatalysts toward toluene were firstly analyzed in the dark condition to understand their PCO performance (Fig. 5a). Interestingly, though exhibiting relatively smaller BET-SSA than pure UiO-66 MOG, the adsorption capacities of the CQDs/UiO-66 composites were greatly improved, and the adsorption capacity of 0.5 wt% CQDs/UiO-66 MOG (29.06 μmol/g) to toluene was 2.1 times that of UiO-66 MOG (13.89 μmol/g). When further increasing the amount of CQDs, the adsorption capacity towards toluene slightly decreased due to the decreased BET-SSA, but it was still higher than UiO-66 MOG. The existence of CQDs might provide new adsorption sites for toluene. In-situ FTIR experiments were performed to verify this conjecture.

In-situ FTIR differential spectra was used to analyze the adsorption process of toluene by UiO-66 MOG and 0.5 wt% CQDs/UiO-66 MOG (Fig. 6). The FTIR signal of the photocatalyst itself has been subtracted as the background. There are some new peaks in the spectra of 0.5 wt% CQDs/UiO-66 MOG. As shown in Fig. 6a, the wavenumber of 3800–3600 cm^{-1} represents the characteristic band of toluene adsorbed by the catalysts, including bridged (3650 cm^{-1}) and terminal hydroxyl groups (3750 and 3729 cm^{-1}) [22]. In Fig. 6b, 1716 and 1697 cm^{-1} represent the vibration of ν(C═O). 1608 and 1517 cm^{-1} are related to the vibration of the benzene ring [22]. 1473, 1435 and 1396 cm^{-1} correspond to the vibrations of $\delta(CH_2)$, $\delta_{as}(CH_3)$, and ν(O—C—O) separately. Furthermore, the interaction between CQDs and toluene was analyzed by in-situ FTIR (Fig. S5). Fig. S5 shows that new peaks at 0.5 wt % CQDs/UiO-66 MOG correspond well with the peaks observed during the adsorption of toluene by pure CQDs, indicating that some toluene molecules were directly adsorbed by CQDs. Therefore, we conclude that CQDs would provide new adsorption sites for toluene in the CQDs/UiO-66 MOG composites.

3.4. Characterization of optical properties and optoelectronic properties

The photoluminescence test is applied to analyze the up-conversion characteristics of CQDs. When excited by long-wavelength light (700–800 nm), CQDs emitted light with wavelength ranging from 275 to 430 nm (Fig. 7a), which could excite UiO-66 MOG. The up-conversion property of CQDs was conducive to applying CQDs/UiO-66 MOG in photocatalysis under visible light. The UV–vis absorption spectra further confirmed the role of CQDs (Fig. 7b). Compared with pure UiO-66 MOG, the CQDs/UiO-66 MOG composites showed stronger light absorption in the visible range. However, a decrease in the light absorption was also observed in the ultra-violet range for the CQDs/UiO-66 MOG samples, especially for 1.0 wt% CQDs/UiO-66 MOG, which might be related to

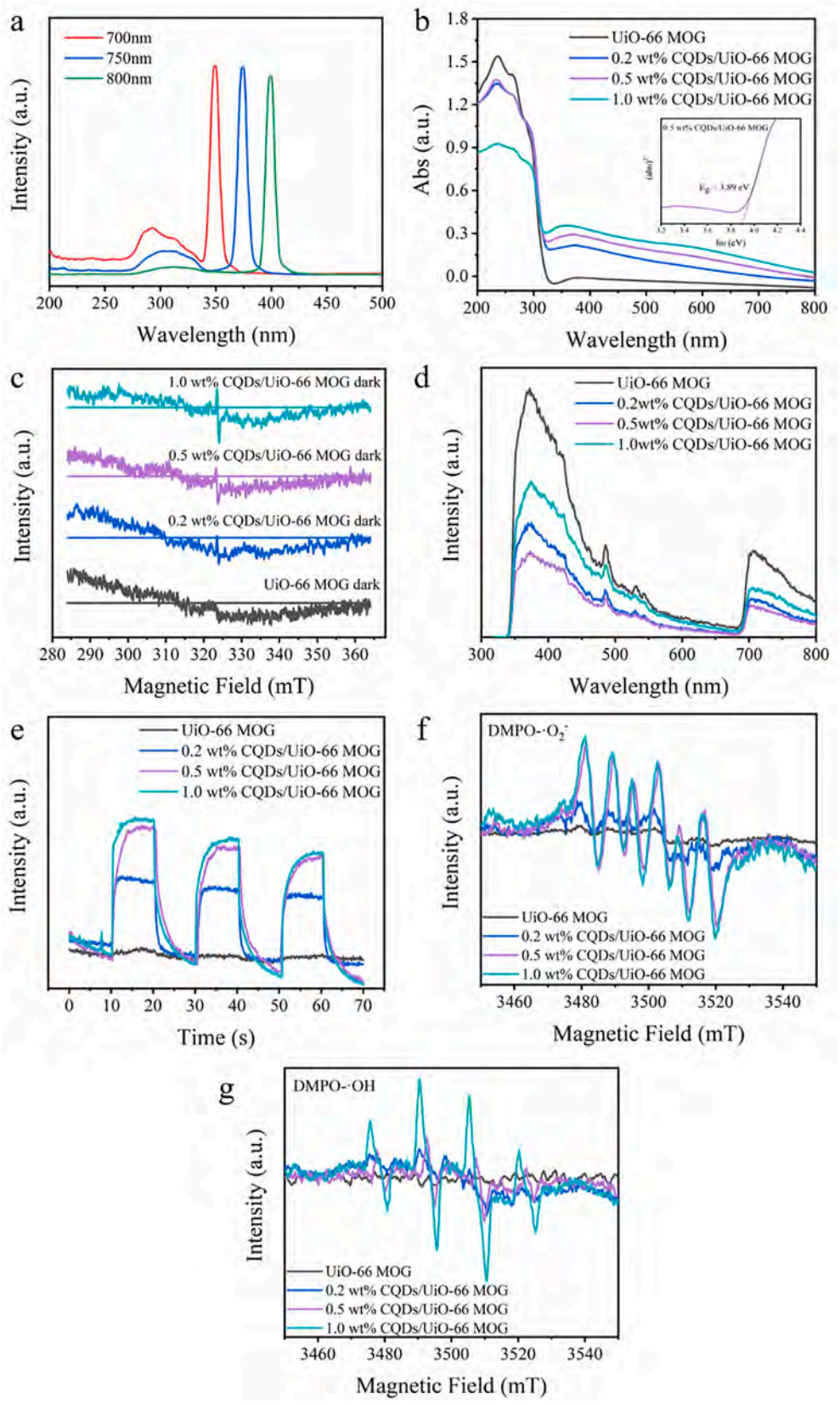

Fig. 7. (a) Up-conversion photoluminescence spectra (UCPL) of CQDs excited by light with different wavelengths. The (b) UV–vis absorption spectra, (c) oxygen vacancies spectra, (d) photoluminescence spectra (PL), (e) cyclic photocurrent response curves and DMPO spin-trapping ESR spectra of (f) $^{\bullet}O_2^-$ (g) $^{\bullet}OH$ of UiO-66 MOG and CQDs/UiO-66 MOG.

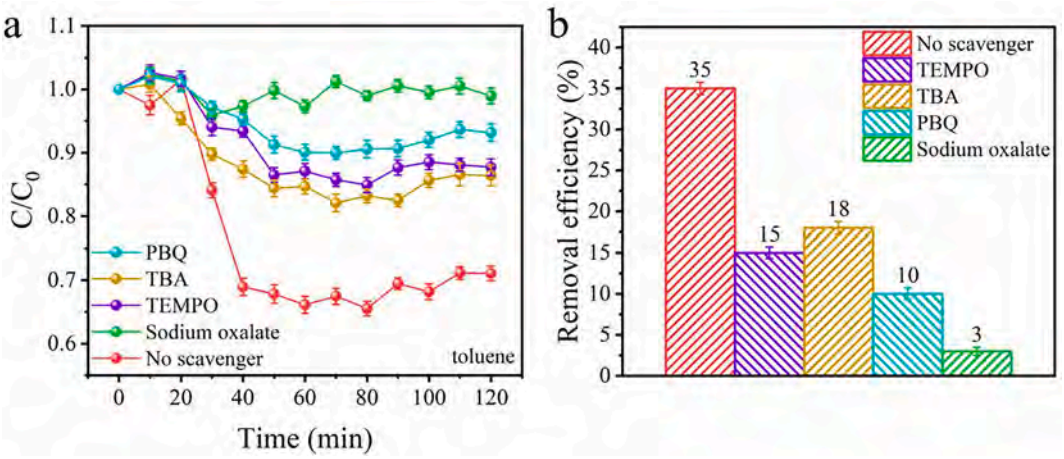

Fig. 8. (a) The photocatalytic degradation curves of toluene captured by the sacrificial agents and (b) The histogram of the degradation efficiency under different active species for 0.5 wt% CQDs/UiO-66 MOG sample, where TEMPO acts as an •OH and $^1O_2$ trapping agent, PBQ acts as an $•O_2^-$ trapping agent, TBA acts as an •OH trapping agent and sodium oxalate acts as a hole trapping agent.

the masking effect of the CQDs.

Aside from the up-conversion effect, the introduction of CQDs was able to generate oxygen vacancies in the substrates [39]. Fig. 7c shows the content of oxygen vacancies in different samples. With the increase of the doping amount of CQDs, the content of oxygen vacancies in the samples increased. A proper increment of oxygen vacancies could enhance the light adsorption and charge separation under visible light, which facilitate the generation of oxidative species, in the same time promote the activation of absorbed O_2 and accelerate the generation of highly oxidative $•O_2^-$ radicals. Therefore, the photocatalytic degradation efficiency of toluene has been improved [40].

In addition to the light absorption ability, the generation and recombination of photogenerated electron-hole pairs in the samples were crucial factors determining photocatalysts' performance. PL spectra (Fig. 7d) indicated the recombination of electron-hole pairs. As an excellent electron acceptor, CQDs could effectively promote the spatial separation of photo-induced electron-hole pairs and significantly reduce the PL intensity of the composites, with 0.5 wt% CQDs/UiO-66 MOG showing the lowest charge carrier recombination efficiency. The extended life-time of electron-hole pairs leads to form more oxidative radicals in which promote the photocatalytic reaction efficiency, on the degradation of gaseous toluene. The CQDs/UiO-66 MOG composites showed much higher photocurrent intensity (Fig. 7e) under visible light than UiO-66 MOG, which confirmed the positive effect of CQDs in the separating charge carriers. ESR spectra (Fig. 7f-g) were used to investigate the content of free radicals generated by the reaction of photogenerated carriers with H_2O and O_2. As showed in Fig. 7f-g, the generation of •OH and $•O_2^-$ radicals were both greatly enhanced with the amount of CQDs increasing. On the one hand, more excited electrons and holes are reserved and react with surface-bond H_2O and O_2. On the other hand, the generation of oxygen vacancies are positive in both adsorption and activation of O_2 to generate $•O_2^-$ [38]. Interestingly, although the most oxidative radicals were generated, the photocatalytic performance of 1.0 wt% CQDs/UiO-66 MOG was still lower than that of 0.5 wt% CQDs/UiO-66 MOG. This phenomenon is possibly related to the role of different radical species in the PCO of toluene and the different absorption properties of the two composites.

In order to further study the contribution of different free radicals in the photocatalytic degradation process, sacrificial agent capture experiments were performed on the 0.5 wt% CQDs/UiO-66 MOG sample. As shown in Fig. 8a, when TEMPO, TBA, PBQ and sodium oxalate were introduced into the PCO system to quench the corresponding free radicals, the degradation efficiency of toluene drops from 35% to 15%, 18%, 10% and 3%, respectively (Fig. 8b). Based on the above results, we confirm that $•O_2^-$ and holes are the main active species in the photodegradation of toluene. This also explains the phenomenon that 1.0 wt% CQDs/UiO-66 MOG produced more free radicals (especially hydroxyl radicals), but showed poorer the degradation efficiency compared with 0.5 wt% CQDs/UiO-66 MOG (Fig. 7f-g).

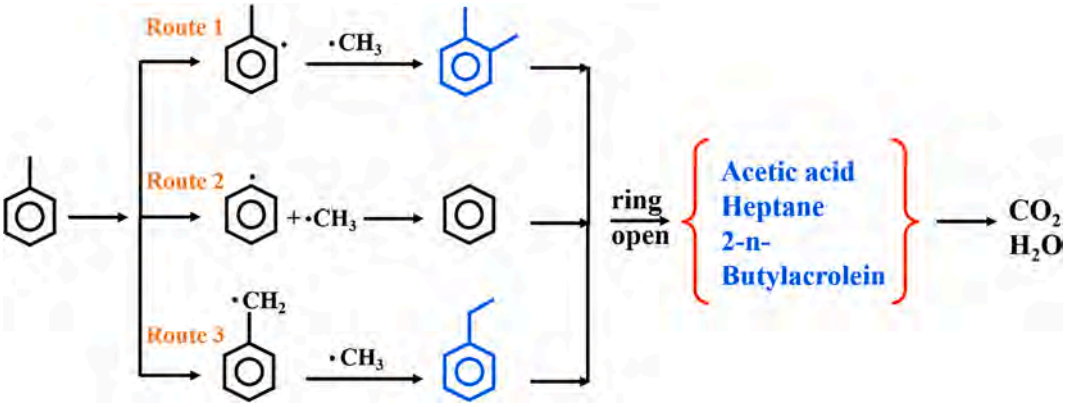

Fig. 9. The proposed photocatalytic degradation pathway of toluene by 0.5 wt% CQDs/UiO-66 MOG, the blue products represent the photodegradation intermediates. (For interpretation of the references to colour in this figure legend, the reader is referred to the web version of this article.)

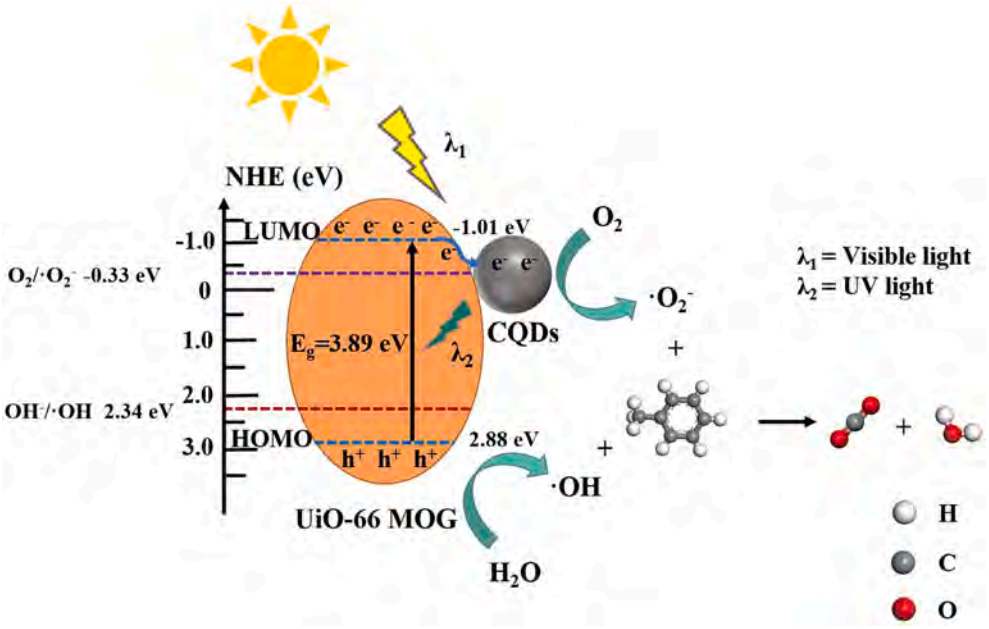

Fig. 10. Photocatalytic mechanism diagram.

3.5. Photocatalytic mechanism

In order to further explore the possible degradation path of toluene on the catalysts, GC–MS method (Fig. S6) was used to study the intermediate products during the process of toluene using 0.5 wt% CQDs/UiO-66 MOG and UiO-66 MOG samples. The types of intermediate products and other information were listed in Table S3. It can be seen from Fig. S6 that after adding CQDs, certain types of accumulated intermediates on the catalysts were no longer detected, which may due to the strong degradation ability of 0.5 wt% CQDs/UiO-66 MOG. Toluene (No. 4) detected in both samples were incompletely degraded reactants absorbed on the catalysts. In addition to toluene, xylene (No. 10, No. 11), ethylbenzene (No. 8) and a small amount of acid (No. 1, No. 2), alcohol (No. 3, No. 13), aldehyde (No. 9) and alkanes (No. 6) were also observed. Therefore, it is speculated that toluene was first converted into xylene or ethylbenzene, aromatic hydrocarbons with lower ring-opening energy. Then xylene and ethylbenzene went through a ring-opening process to form acids, alcohols, aldehydes, etc., which were finally mineralized into CO_2 and H_2O (Fig. 9). As indicated by Fig. 9, the oxidative radicals (H^+, $\bullet O_2^-$, $\bullet OH$) may attack the benzene ring or the methyl group of toluene to form intermediates such as xylene and ethylbenzene. As shown by Route 2 in Fig. 9, during the generation of methyl radicals, benzene is also produced [38]. However, the presence of benzene was not detected in GC–MS, due to the strong π-π interaction between benzene and the linker of UiO-66, which made it hard for benzene to desorb from the catalysts.

Based on the analysis above, we proposed the mechanism of CQDs to improve the photocatalytic performance of CQDs/UiO-66 MOG (Fig. 10). 0.5 wt% CQDs/UiO-66 MOG showed the best performance in the photocatalytic elimination of toluene, which can be concluded in the following aspects: i) by introducing new active sites into the CQDs/UiO-66 MOG samples, CQDs could effectively improve the adsorption of toluene, which is essential for the following PCO processes; ii) CQDs promoted the generation and separation of photogenerated carriers due to its up-conversion effect and excellent conductivity, which was conducive to the generation of free radicals; iii) through introducing oxygen vacancy into UiO-66 MOG, the addition of CQDs promoted the activation of absorbed O_2 and the generation of $\bullet O_2^-$ radicals, which plays a dominant role in the oxidative degradation of toluene.

4. Conclusion

In summary, CQDs/UiO-66 MOGs with hierarchical pore structures were synthesized by a quasi-in-situ method. They can effectively degrade toluene under visible light. In addition, the 0.5 wt% CQDs/UiO-66 MOG exhibited high CO_2 conversion during the degradation of toluene, thus reducing the generation of toxic intermediates. The CQDs act as a photosensitizer to improve the light utilization efficiency of the samples. At the same time, the excellent conductivity of CQDs enables the spatial separation of photogenerated charge carriers. Moreover, the number of oxygen vacancies in the samples containing CQDs increased after light exposure, which is conducive to the generation of $\bullet O_2^-$ radicals and the photocatalytic degradation. Holes and superoxide radicals were found to play a major role in the reaction. The possible degradation pathways of toluene were proposed. This work analyzed the degradation process of CQDs/UiO-66 MOG to toluene, and provided new ideas for the optimizing and application of zirconium-based MOG in the degradation of gaseous VOCs.

Declaration of Competing Interest

The authors declare that they have no known competing financial interests or personal relationships that could have appeared to influence the work reported in this paper.

Acknowledgments

This work was financially supported by the Key Collaborative Research Program of the Alliance of International Science Organizations (Grant. No. ANSO-CR-KP-2020-13); the National Key Research and Development Program of China (2021YFE0110400); the National Natural Science Foundation of China (41907303, 52072387) ; Shanghai Commission of Science and Technology Program (19DZ1202600, 20DZ1204100); the State Key Laboratory Director Fund of SICCAS (Y9ZC0102).

Appendix A. Supplementary data

Supplementary data to this article can be found online at https://doi.org/10.1016/j.cej.2022.135033.

References

[1] C. Lai, Z. Wang, L. Qin, Y. Fu, B. Li, M. Zhang, S. Liu, L. Li, H. Yi, X. Liu, X. Zhou, N. An, Z. An, X. Shi, C. Feng, Metal-organic frameworks as burgeoning materials for the capture and sensing of indoor VOCs and radon gases, Coord. Chem. Rev. 427 (2021), 213565.

[2] X. Qiu, Y. Zhang, Y. Zhu, C. Long, L. Su, S. Liu, Z. Tang, Applications of nanomaterials in asymmetric photocatalysis: recent progress, challenges, and opportunities, Adv. Mater. 33 (2021).

[3] R. Chen, J. Li, J. Sheng, W. Cui, X. Dong, P. Chen, H. Wang, Y. Sun, F. Dong, Unveiling the unconventional roles of methyl number on the ring-opening barrier in photocatalytic decomposition of benzene, toluene and o-xylene, Appl. Catal. B 278 (2020).

[4] L. Wang, H. Xu, J. Gao, J. Yao, Q. Zhang, Recent progress in metal-organic frameworks-based hydrogels and aerogels and their applications, Coord. Chem. Rev. 398 (2019).

[5] Y.u. Shen, T. Pan, L. Wang, Z. Ren, W. Zhang, F. Huo, Programmable logic in metal-organic frameworks for catalysis, Adv. Mater. (2021).

[6] P.J. Jodlowski, G. Kurowski, L. Kuterasinski, M. Sitarz, P. Jelen, J. Jaskowska, A. Kolodziej, A. Pajdak, Z. Majka, A. Boguszewska-Czubara, Cracking the chloroquine conundrum: the application of defective UiO-66 metal-organic framework materials to prevent the onset of heart defects-in vivo and in vitro, ACS Appl. Mater. Interfaces 13 (2021) 312–323.

[7] X.-Y. Xu, C. Chu, H. Fu, X.-D. Du, P. Wang, W. Zheng, C.-C. Wang, Light-responsive UiO-66-NH2/Ag3PO4 MOF-nanoparticle composites for the capture and release of sulfamethoxazole, Chem. Eng. J. 350 (2018) 436–444.

[8] K. Jayaramulu, F. Geyer, A. Schneemann, Š. Kment, M. Otyepka, R. Zboril, D. Vollmer, R.A. Fischer, Hydrophobic metal-organic frameworks, Adv. Mater. (2019) 31.

[9] X. Zhang, G. Li, D. Wu, X. Li, N. Hu, J. Chen, G. Chen, Y. Wu, Recent progress in the design fabrication of metal-organic frameworks-based nanozymes and their applications to sensing and cancer therapy, Biosens. Bioelectron. 137 (2019) 178–198.

[10] Z. Rao, G. Lu, A. Mahmood, G. Shi, X. Xie, J. Sun, Deactivation and activation mechanism of TiO2 and rGO/Er3+-TiO2 during flowing gaseous VOCs photodegradation, Appl. Catal. B 284 (2021).

[11] D.-W. Lim, H. Kitagawa, Rational strategies for proton-conductive metal-organic frameworks, Chem. Soc. Rev. 50 (2021) 6349–6368.

[12] M. Jia, W. Xiong, Z. Yang, J. Cao, Y. Zhang, Y. Xiang, H. Xu, P. Song, Z. Xu, Metal-organic frameworks and their derivatives-modified photoelectrodes for photoelectrochemical applications, Coord. Chem. Rev. 434 (2021).

[13] F.X.L.I. Xamena, A. Corma, H. Garcia, Applications for metal−organic frameworks (MOFs) as quantum dot semiconductors, J. Phys. Chem. C 111 (2007) 80–85.

[14] L. Zhang, X. Shi, Z. Zhang, R.P. Kuchel, R. Namivandi-Zangeneh, N. Corrigan, K. Jung, K. Liang, C. Boyer, Porphyrinic zirconium metal-organic frameworks (MOFs) as heterogeneous photocatalysts for PET-RAFT polymerization and stereolithography, Angew. Chem. Int. Ed. 60 (2021) 5489–5496.

[15] H. Hu, Z. Wang, L. Cao, L. Zeng, C. Zhang, W. Lin, C. Wang, Metal-organic frameworks embedded in a liposome facilitate overall photocatalytic water splitting, Nat. Chem. 13 (2021).

[16] L.u. Chen, X. Wang, Z. Rao, Z. Tang, Y. Wang, G. Shi, G. Lu, X. Xie, D. Chen, J. Sun, In-situ synthesis of Z-Scheme MIL-100(Fe)/α-Fe2O3 heterojunction for enhanced adsorption and Visible-light photocatalytic oxidation of O-xylene, Chem. Eng. J. 416 (2021).

[17] X.-M. Cheng, X.-Y. Dao, S.-Q. Wang, J. Zhao, W.-Y. Sun, Enhanced photocatalytic CO2 reduction activity over NH2-MIL-125(Ti) by facet regulation, ACS Catal. 11 (2021) 650–658.

[18] J. Hou, A.F. Sapnik, T.D. Bennett, Metal-organic framework gels and monoliths, Chem Sci 11 (2020) 310–323.

[19] X. Zheng, H. Zhang, S. Rehman, P. Zhang, Energy-efficient capture of volatile organic compounds from humid air by granular metal organic gel, J. Hazard. Mater. 411 (2021).

[20] J.H. Cavka, S. Jakobsen, U. Olsbye, N. Guillou, C. Lamberti, S. Bordiga, K. P. Lillerud, A new zirconium inorganic building brick forming metal organic frameworks with exceptional stability, J. Am. Chem. Soc. 130 (2008) 13850–13851.

[21] F. Bi, X. Zhang, J. Chen, Y. Yang, Y. Wang, Excellent catalytic activity and water resistance of UiO-66-supported highly dispersed Pd nanoparticles for toluene catalytic oxidation, Appl. Catal. B 269 (2020).

[22] J. Zhang, Z. Guo, Z. Yang, J. Wang, J. Xie, M. Fu, Y. Hu, TiO_2@UiO-66 composites with efficient adsorption and photocatalytic oxidation of VOCs: investigation of synergistic effects and reaction mechanism, ChemCatChem 13 (2020) 581–591.

[23] S.Y. Lim, W. Shen, Z. Gao, Carbon quantum dots and their applications, Chem. Soc. Rev. 44 (2015) 362–381.

[24] T. Zhou, S. Chen, L. Li, J. Wang, Y. Zhang, J. Li, J. Bai, L. Xia, Q. Xu, M. Rahim, B. Zhou, Carbon quantum dots modified anatase/rutile TiO2 photoanode with dramatically enhanced photoelectrochemical performance, Appl. Catal. B 269 (2020).

[25] Y. Li, Z. Liu, Y. Wu, J. Chen, J. Zhao, F. Jin, P. Na, Carbon dots-TiO2 nanosheets composites for photoreduction of Cr(VI) under sunlight illumination: favorable role of carbon dots, Appl. Catal. B 224 (2018) 508–517.

[26] A. Mahmood, G. Shi, Z. Wang, Z. Rao, W. Xiao, X. Xie, J. Sun, Carbon quantum dots-TiO2 nanocomposite as an efficient photocatalyst for the photodegradation of aromatic ring-containing mixed VOCs: An experimental and DFT studies of adsorption and electronic structure of the interface, J. Hazard. Mater. (2021).

[27] S. Qu, X. Wang, Q. Lu, X. Liu, L. Wang, A biocompatible fluorescent ink based on water-soluble luminescent carbon nanodots, Angew. Chem. Int. Ed. 51 (2012) 12215–12218.

[28] B. Bueken, N. Van Velthoven, T. Willhammar, T. Stassin, I. Stassen, D.A. Keen, G. V. Baron, J.F.M. Denayer, R. Ameloot, S. Bals, D. De Vos, T.D. Bennett, Gel-based morphological design of zirconium metal-organic frameworks, Chem. Sci. 8 (2017) 3939–3948.

[29] L. Valenzano, B. Civalleri, S. Chavan, S. Bordiga, M.H. Nilsen, S. Jakobsen, K. P. Lillerud, C. Lamberti, Disclosing the complex structure of UiO-66 metal organic framework: a synergic combination of experiment and theory, Chem. Mater. 23 (2011) 1700–1718.

[30] J. Santos-Lorenzo, R. San José-Velado, J. Albo, G. Beobide, P. Castaño, O. Castillo, A. Luque, S. Pérez-Yáñez, A straightforward route to obtain zirconium based metal-organic gels, Microporous Mesoporous Mater. 284 (2019) 128–132.

[31] X. Miao, D. Qu, D. Yang, B. Nie, Y. Zhao, H. Fan, Z. Sun, Synthesis of carbon dots with multiple color emission by controlled graphitization and surface functionalization, Adv. Mater. 30 (2018).

[32] V. Tucureanu, A. Matei, A.M. Avram, FTIR spectroscopy for carbon family study, Crit. Rev. Anal. Chem. 46 (2016) 502–520.

[33] P. Chen, F. Wang, Z.-F. Chen, Q. Zhang, Y. Su, L. Shen, K. Yao, Y. Liu, Z. Cai, W. Lv, G. Liu, Study on the photocatalytic mechanism and detoxicity of gemfibrozil by a sunlight-driven TiO2/carbon dots photocatalyst: the significant roles of reactive oxygen species, Appl. Catal. B 204 (2017) 250–259.

[34] S. Zhuang, R. Cheng, J. Wang, Adsorption of diclofenac from aqueous solution using UiO-66-type metal-organic frameworks, Chem. Eng. J. 359 (2019) 354–362.

[35] F.G. Cirujano, N. Martin, L.H. Wee, Design of hierarchical architectures in metal-oganic frameworks for catalysis and adsorption, Chem. Mater. 32 (2020) 10268–10295.

[36] C. Chen, D. Chen, S. Xie, H. Quan, X. Luo, L. Guo, Adsorption behaviors of organic micropollutants on zirconium metal-organic framework UiO-66: analysis of surface interactions, ACS Appl. Mater. Interfaces 9 (2017) 41043–41054.

[37] P. Hu, X. Liang, M. Yaseen, X. Sun, Z. Tong, Z. Zhao, Z. Zhao, Preparation of highly-hydrophobic novel N-coordinated UiO-66(Zr) with dopamine via fast mechano-chemical method for (CHO-/Cl-)-VOCs competitive adsorption in humid environment, Chem. Eng. J. 332 (2018) 608–618.

[38] Z. Rao, G. Shi, Z. Wang, A. Mahmood, X. Xie, J. Sun, Photocatalytic degradation of gaseous VOCs over Tm3+-TiO2: revealing the activity enhancement mechanism and different reaction paths, Chem. Eng. J. 395 (2020).

[39] N. Prasetya, B.P. Ladewig, An insight into the effect of azobenzene functionalities studied in UiO-66 frameworks for low energy CO2 capture and CO2/N-2 membrane separation, J. Mater. Chem. A 7 (2019) 15164–15172.

[40] X. Dong, W. Cui, H. Wang, J. Li, Y. Sun, H. Wang, Y. Zhang, H. Huang, F. Dong, Promoting ring-opening efficiency for suppressing toxic intermediates during photocatalytic toluene degradation via surface oxygen vacancies, Sci. Bull. 64 (2019) 669–678.